Advanced Composite Materials
Publication details, including instructions for authors and subscription information:
http://www.tandfonline.com/loi/tacm20

Impact damage and residual tensile strength of a CF-SMC composite

Keiji Ogi [a], Jang-Woo Kim [b], Kousei Ono [c] & Nobuhide Uda [c]

[a] Graduate School of Science and Engineering, Ehime University, 3, Bunkyocho, Matsuyama, Ehime, 790-8577, Japan

[b] Graduate School of Engineering, Osaka University, 1-1 Yamadaoka, Suita, Osaka, 565-0871, Japan

[c] Faculty of Engineering, Kyushu University, 744 Motooka, Nishi-ku, Fukuoka, 819-0395, Japan

Published online: 04 Feb 2013.

To cite this article: Keiji Ogi, Jang-Woo Kim, Kousei Ono & Nobuhide Uda (2013) Impact damage and residual tensile strength of a CF-SMC composite, Advanced Composite Materials, 22:1, 29-47, DOI: 10.1080/09243046.2013.764779

To link to this article: http://dx.doi.org/10.1080/09243046.2013.764779

Advanced Composite Materials, 2013
Vol. 22, No. 1, 29–47, http://dx.doi.org/10.1080/09243046.2013.764779

Taylor & Francis
Taylor & Francis Group

Impact damage and residual tensile strength of a CF-SMC composite

Keiji Ogi[a]*, Jang-Woo Kim[b], Kousei Ono[c] and Nobuhide Uda[c]

[a]*Graduate School of Science and Engineering, Ehime University, 3, Bunkyocho, Matsuyama, Ehime 790-8577, Japan;* [b]*Graduate School of Engineering, Osaka University, 1-1 Yamadaoka, Suita, Osaka 565-0871, Japan;* [c]*Faculty of Engineering, Kyushu University, 744 Motooka, Nishi-ku, Fukuoka 819-0395, Japan*

(*Received 29 May 2012; accepted 7 January 2013*)

In this study, the impact damage and the tension after impact (TAI) strength of a carbon-fiber-reinforced sheet molding compound (CF-SMC) are analyzed. First, low-velocity impact damage is introduced to several CF-SMC coupon specimens for a variety of impact energies. Next, the impact damage is observed by ultrasonic inspection and optical microscopy to determine the damage state and quantify the damage area and depth. Then, the TAI strength is measured and correlated with such parameters as maximum impact load, impact energy, and damage area and depth. Finally, a simple fracture-mechanics model for predicting the TAI strength is proposed. It is proved that the TAI strength depends on the impact damage depth.

Keywords: sheet molding compound; impact behavior; nondestructive testing; ultrasonics

1. Introduction

Carbon-fiber-reinforced plastics (CFRPs) have recently been used for lightweight structural components of transportation machinery to improve fuel consumption. It is assumed that reducing the weight of an automotive body by 30% reduces life cycle energy consumption by 20%. In applying CFRPs to automobiles, both formability and short production time are required for mass production. Therefore, press molding is usually adopted when sheet molding compound (SMC) composites are applied to automobiles. In particular, carbon-fiber-reinforced SMC (CF-SMC) composites are promising automotive structural materials because they have better mechanical properties (e.g. high specific strength and modulus) than glass fiber SMCs (GF-SMCs).

To date, several researchers have investigated the strength and fracture of GF- and CF-SMCs. Fernberg and J*ēkabsons* [1,2] used the bridging laws, or fracture process zone laws, to predict progressive failure of GF-SMCs. Other studies have been conducted on flexural strength,[3] the probabilistic failure model,[4] and micromechanical models [5,6] of SMCs. Recently, the authors [7,8] developed fracture-mechanics models for predicting the tensile and flexural strength of a CF-SMC by modifying the model for unidirectional arrayed chopped strands (UACSs) [9,10] that exhibit fracture characteristics similar to those of the CF-SMC. They reported that the strength of the CF-SMC depends on the size of the damage generated at the early stage of loading (*initial damage*) and specimen dimensions (thickness and width),

*Corresponding author. Email: ogi.keiji.mu@ehime-u.ac.jp

and that the variability of the flexural strength is also related to the variation of initial damage location.

Several studies have been performed on impact damage and residual strength after impact of SMC composites.[11–18] For example, Lee et al. [12] measured the dissipated impact energy of SMC composites to examine the effect of mass and shape of impactor, initial velocity, and specimen thickness on the impact characteristics. Dear and Brown [13] investigated the damage processes of a SMC to correlate them with load–displacement and absorbed energy data. Chaturvedi and Sierakowski [16] proposed a fracture-mechanics model for predicting the residual strength of impacted GF-SMC composites, considering energy dissipation associated with damage. Since the microstructure of a SMC is coarse, the strength of a SMC is strongly affected by intrinsic damage or defects on a millimeter scale.[3] Hence, it is reasonable to predict the residual strength of impacted SMC composites in light of fracture mechanics. Therefore, to precisely predict the tension after impact (TAI) strength, it is necessary to quantitatively evaluate three-dimensionally distributed impact damage.

This study seeks to characterize the impact damage and to investigate the TAI of a CF-SMC composite. First, a low-velocity impact load was applied to composite specimens to induce impact damage. Next, impact damage was observed using ultrasonic inspection and optical microscopy. The impact damage area was measured from the C-scan images. Tensile tests were then performed for the impacted specimens to measure the TAI strength. The correlation between the TAI strength and maximum impact load, maximum deflection, incident impact energy, absorbed energy, and impact damage area was examined next. In addition, internal damage progress up to final failure during the tensile test was analyzed using soft X-ray radiography. Damage extension on the edge surface was also observed by optical microscopy. Finally, a simple formulation was proposed to predict the TAI strength based on fracture mechanics.

2. Experimental procedure

2.1. Material

A SMC made out of carbon fiber and vinyl ester resin was used in this study. The CF-SMC plates were cured at 130 °C in the press-molding process. The weight fraction of CF was 50%. The chopped strands, which consisted of 12,000 carbon filaments, were 25.4 mm long, 6 mm wide, and 0.3 mm thick before fabrication. Due to pressing, the thickness of the chopped strands after fabrication varies from 0.1 to 0.4 mm. This variation also causes the width to vary from 4.5 to 18 mm, assuming that the length and volume of the chopped strands remain constant.

Figure 1 schematically illustrates a CF-SMC. The irregularly shaped chopped strands are randomly oriented, lying on top of one another. An interlaminar region exists between the strands, as well as in a multidirectional continuous fiber laminate. As a result, damage modes, such as matrix cracking and delamination, are analogous to those of a multidirectional laminate, although the final failure mode is not fiber breakage but delamination or splitting.[7,8]

The CF-SMC plates were cut into 17 coupon specimens 130 mm long, 25.4 mm wide, and 3.0 mm thick. Ten specimens were employed for the impact tests, while the rest of the specimens were used to measure the initial tensile strength and Young's modulus. After the impact test and ultrasonic inspection, 25-mm-long GFRP doublers were adhesively bonded to the specimens for the subsequent tensile test. Table 1 lists the mechanical properties of the CF-SMC.[7,8] Variations of the strength and modulus are relatively large compared with those of a continuous fiber laminate, mainly because the strength depends on the size of *initial damage* that is generated at the interfaces of the strands at a low stress level.[7,8]

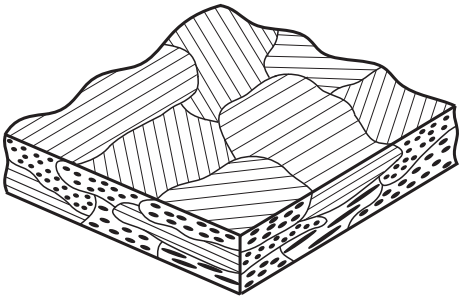

Figure 1. Schematic of a CF-SMC.

Table 1. Properties of a CF-SMC composite.[7,8]

	Tensile strength σ_{T0} (MPa)	Flexural strength σ_{F0} (MPa)	Elastic modulus E_{SMC} (GPa)	Mode-II interlaminar fracture toughness G_{IIC} (J/m^2)
	149	312	33.9	600
Coefficient of variation	0.13	0.17	0.12	N/A

2.2. Impact test

Low-velocity impact tests were performed using a drop-weight impact-testing machine (Dynatup 9210, Instron). Figure 2 presents a photograph and a schematic of the specimen setup. Both edges of a CF-SMC specimen were rigidly clamped between two jig plates with a 76-mm-diameter circular hole. The impactor is a circular rod with a 16-mm-diameter hemispherical aluminum tip. The impactor weighed 1.1 kg. The impact load, impact velocity, and specimen displacement were measured with the instrumented impactor. The incident impact energy varied from 1.1 to 3.5 J by adjusting the drop height of the impactor from 10.5 to 32.3 cm. The energy absorbed in the specimen was calculated from the incident and rebound velocities of the impactor. The incident impact energy, absorbed energy, and impact velocity for each specimen are listed in Table 2. Any damage losses due to friction are not considered here.

2.3. Impact damage observation

Internal impact damage was nondestructively evaluated using ultrasonography (G-SCAN 6AX500, GNES), which allowed us to detect damage near the back surface by adjusting the acoustic wave sensitivity depending on the depth.[19] Ultrasonic inspection was conducted from both impacted (front) and back surfaces using an acoustic wave probe with a frequency of 15 MHz, at a scanning pitch of 0.2 mm × 0.2 mm. Planar images (C-scope) and tomographic images (B-scope) were obtained for an area of 50 mm × 25 mm around the impact point. For C-scope in particular, images were taken in both ECHO and Beam Path Measurement (BPM) modes. The ECHO mode image is based on the intensity of the echo, while the BPM mode image reflects the depth of the echo. In addition, Specimen No. 10, which was impacted by the greatest energy, was cut in a plane that passed through the impact point to observe the detailed internal damage using an optical microscope.

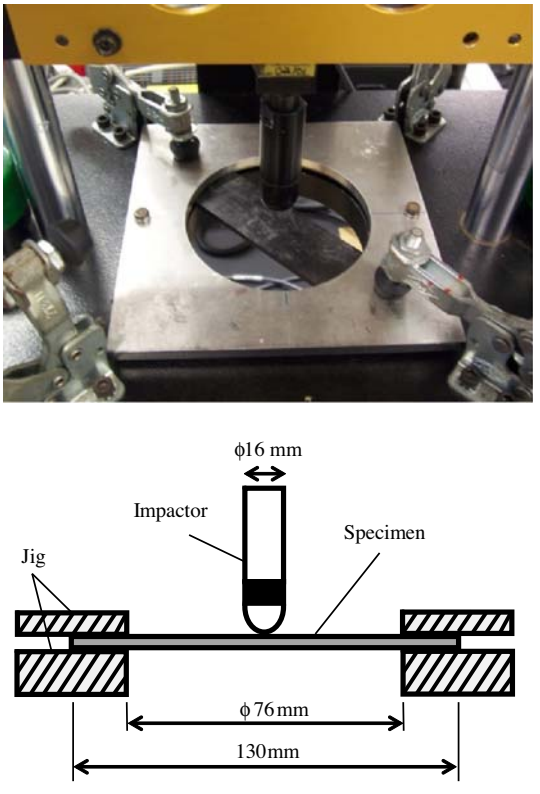

Figure 2. Configuration of specimen setup in the impact test.

Table 2. Summary of impact test.

Specimen number	Incident energy E_{in} (J)	Impact velocity v (m/s)	Absorbed energy E_{ab} (J)	Maximum deflection d_{max} (mm)	Maximum load F_{max} (kN)
1	1.14	1.44	0.794	2.57	0.700
2	1.74	1.78	1.03	3.20	0.935
3	1.73	1.78	0.959	3.10	0.964
4	1.77	1.79	1.31	3.46	0.885
5	2.29	2.04	1.87	4.78	0.817
6	2.27	2.03	1.31	3.59	1.08
7	2.35	2.07	1.68	3.68	1.080
8	2.26	2.03	1.60	3.43	1.05
9	2.94	2.31	2.60	6.53	0.851
10	3.48	2.52	N/A (2.43)*	3.46	0.944

Note: *N/A denotes failure in data acquisition. The value in parenthesis is estimated by linear approximation of the experiment results.

2.4. *Tensile test and observation of damage evolution*

Tensile tests were performed at room temperature and at a loading speed of 0.5 mm/min using a hydraulic testing machine (INSTRON 8516), except for Specimen No. 10, where the damage on the cross section was observed. Moreover, the tensile test was stopped at several loads

to observe damage evolution for the two specimens impacted at low and high energy (Specimen Nos. 2 and 8). The damage on the edge was detected using optical microscopy, and the damage inside of the specimens was detected using soft X-ray radiography (M-100, SOFTEX). A contrast medium containing zinc iodide was injected into the specimen to obtain a clear radiograph of the damage.

3. Results and discussion

3.1. Impact characteristics

Figure 3 depicts typical results of load–time, energy stored in the specimen–time and load–displacement diagrams. Load and stored energy increase nonlinearly with time up to the maximum values, whereas the time to the maximum energy, or incident impact energy E_{in}, is slightly behind the time to the maximum load. When the load reaches zero, the stored energy evolves to a constant value defined as the absorbed energy, E_{ab}. The load–displacement curve is approximately linear for small deflection (<1.5 mm) but becomes nonlinear as deflection increases. Figure 4 plots the load–displacement curves of specimens impacted at various incident impact energies. Maximum load and deflection increase with an increasing incident energy, as long as the results of Specimen Nos. 1, 3, and 7 are compared (Figure 4(a)). However, maximum load does not always increase with increasing incident energy when impact energy becomes greater (Figure 4(b)). Specimen Nos. 5 and 7, which are subjected to almost the same impact energy (2.3 J), exhibit quite different load–displacement diagrams: namely, Specimen No. 5 is ductile, which results in it having an absorbed energy slightly higher than that of Specimen No. 7.

Figure 5(a) presents the relationship between the maximum impact load and deflection. These values are added to Table 2. The maximum impact load increases almost linearly for deflection less than 3.5 mm but decreases for greater deflection. Figure 5(b) plots absorbed energy and maximum impact load against incident energy. The absorbed energy is approximately proportional to the incident energy with a proportionality factor of 0.7. However, the maximum load is not proportional to impact energy. It decreases at impact energies exceeding 2.3 J. This nonlinearity is presumably due to accumulation of microscopic damage.

3.2. Impact damage

Figure 6 presents legends of colors in ECHO and BPM mode images. In the ECHO mode images, red denotes the damage area with high-intensity echo, while blue denotes the intact area with low-intensity echo. In the BPM mode images, the echoes from the front surface are denoted by black, and those from the back surface are denoted by red.

C-scope images (ECHO and BPM modes) and B-scope images for Specimen Nos. 2, 3, 5, 7, 8, 9, and 10 are tabulated in Figure 7. For all specimens except No. 9, only C-scope images inspected from the back surface are presented in Figures 7(a)–(c); however, C-scope images of Specimen No. 9 (Figure 7(d)) were obtained by inspection from both front and back surfaces. In all the images, the lateral direction represents the length direction. The vertical direction represents the thickness direction in B-scope images and the width direction in C-scope images. The white area in the C-scope images of Specimen Nos. 9 and 10 represents the nonplanar part resulting from permanent bending deformation. The shape of the damage is irregular, not spiral, as is observed in a quasi-isotropic laminate.[19] In addition, impact damage tends to propagate in the width direction because the specimen has a coupon shape rather than a square shape. Hereafter, the discussion focuses on damage area and depth that can affect residual strength.

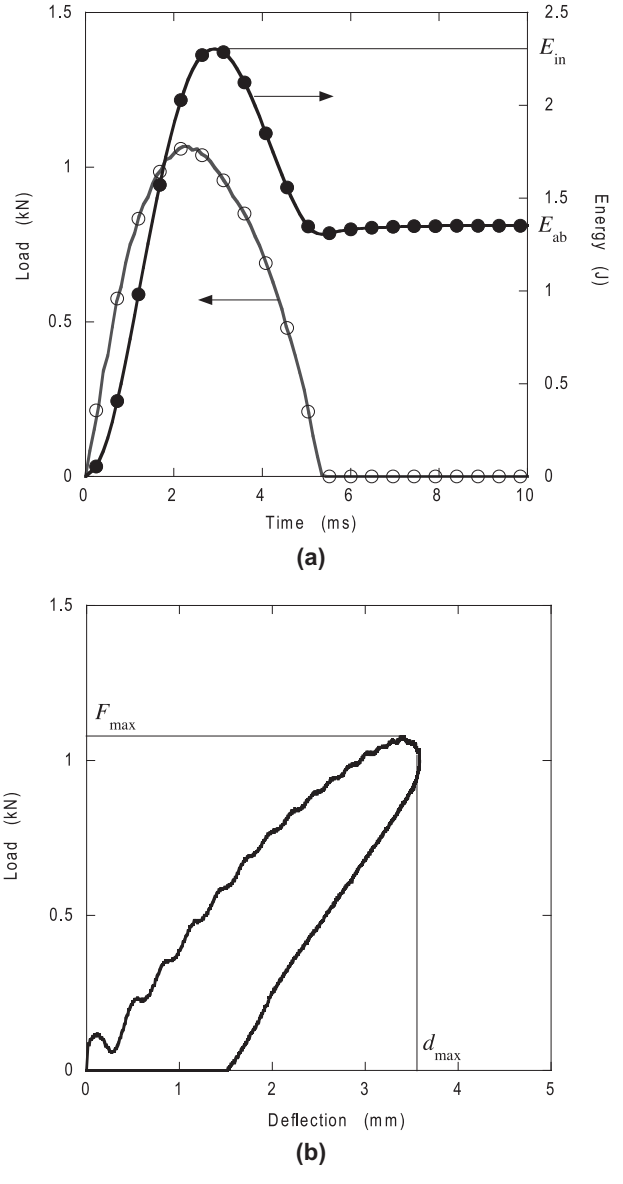

Figure 3. Typical (a) load–time and energy stored in the specimen–time diagrams and (b) load–displacement curve (Specimen No. 6).

Table 3 summarizes the damage area. In most specimens, the damage area inspected from the back surface is larger than that observed from the front surface. Generally, impact damage expands from the front surface toward the back surface in a conical shape. Therefore, the echoes caused by damage are more sensitively detected when inspected from the back surface. This characteristic is also found in the optical micrograph of the cross section in Figure 8, where matrix cracks as well as cracks at the strand edges are connected with each other by delamination.

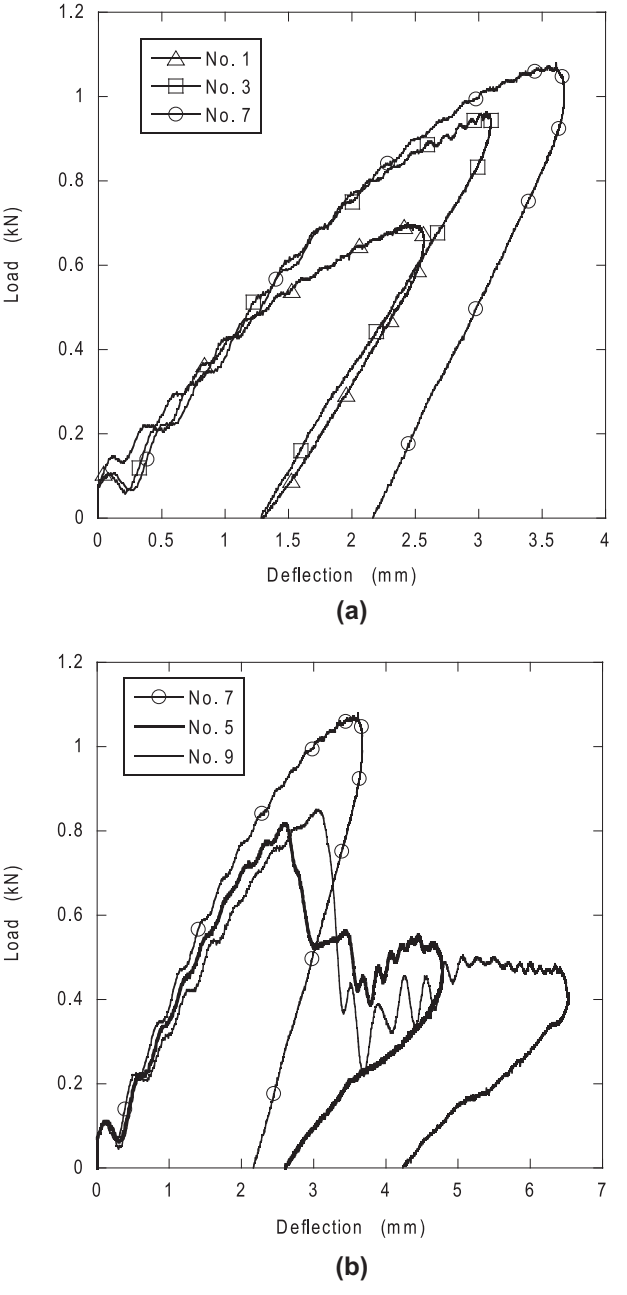

Figure 4. Load–displacement curves of specimens impacted at various impact energies. (a) Specimen Nos. 1, 3, and 7 and (b) Specimen Nos. 5, 7, and 9.

Figure 9 depicts the damage area calculated using C-scan (ECHO mode) images observed from the front and back surfaces, plotted as a function of maximum impact load, maximum deflection, incident impact energy, and absorbed energy. The maximum deflection (threshold 3.5 mm), incident impact energy (threshold 2.0 J), and absorbed energy (threshold 1.3 J) are

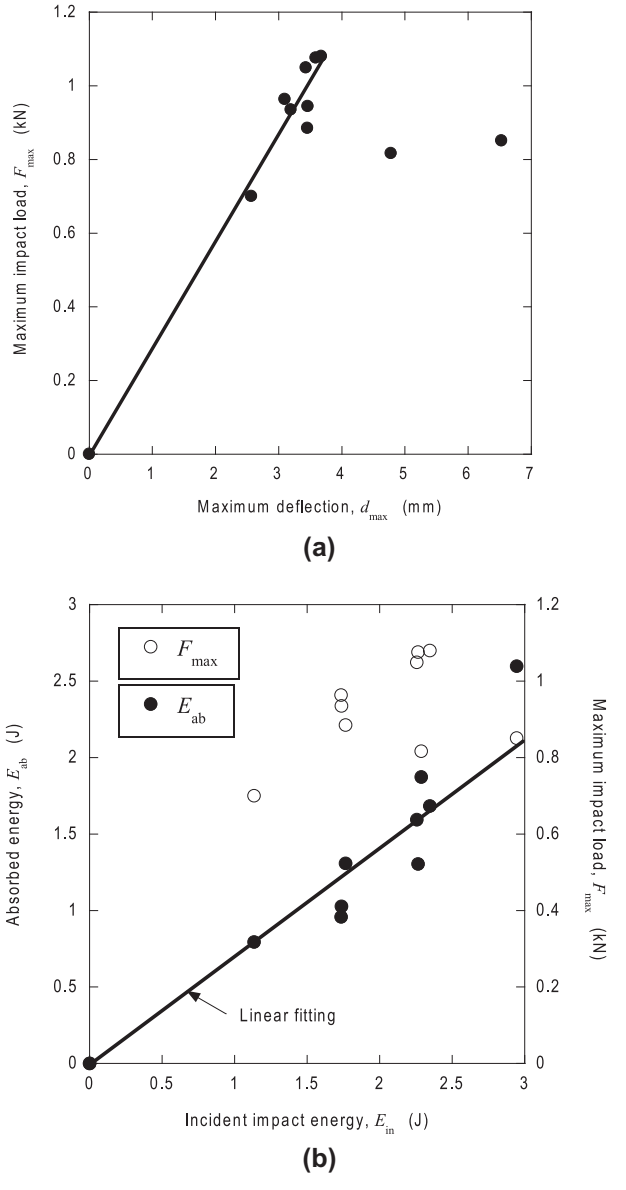

Figure 5. (a) Maximum impact load vs. maximum deflection and (b) absorbed energy and maximum impact load vs. incident impact energy.

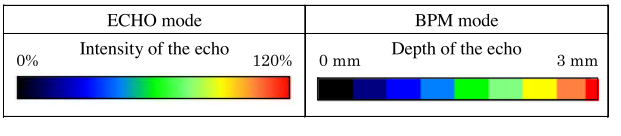

Figure 6. Legends for the C-scope images in Figure 7.

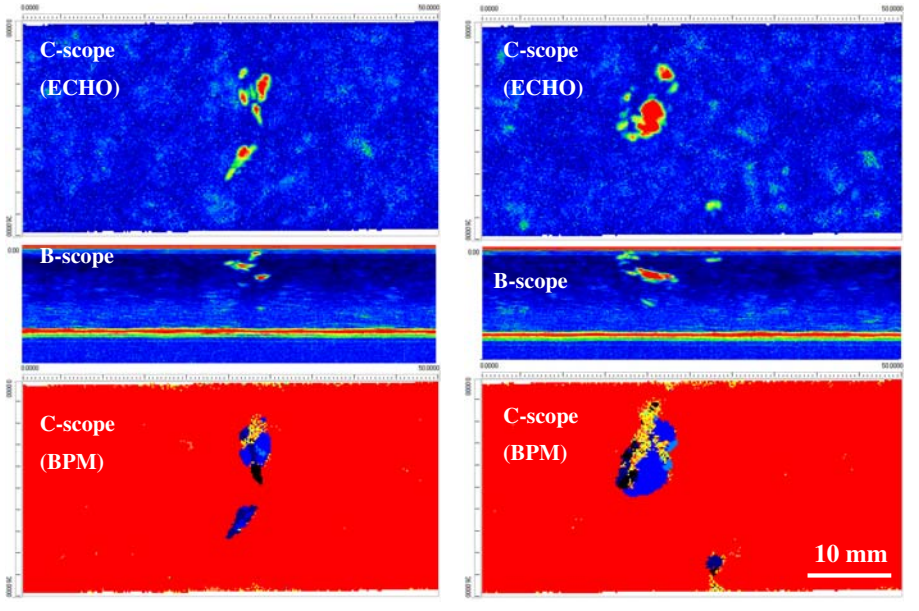

No. 2 No. 3

(a)

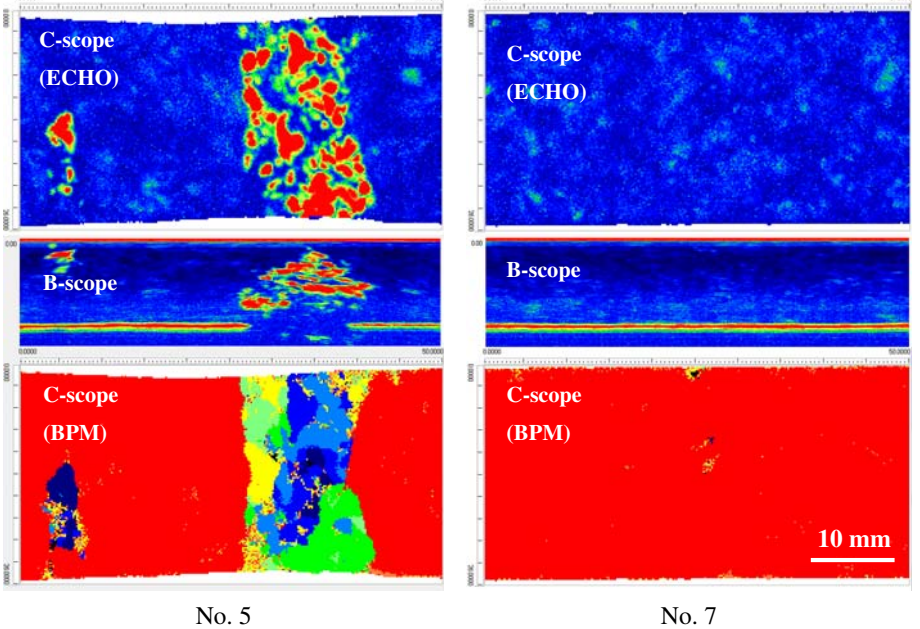

No. 5 No. 7

(b)

Figure 7. Ultrasonic inspection images of impacted specimens. (a) Specimen Nos. 2 and 3; (b) Specimen Nos. 5 and 7; (c) Specimen Nos. 8 and 10; and (d) Specimen No. 9.

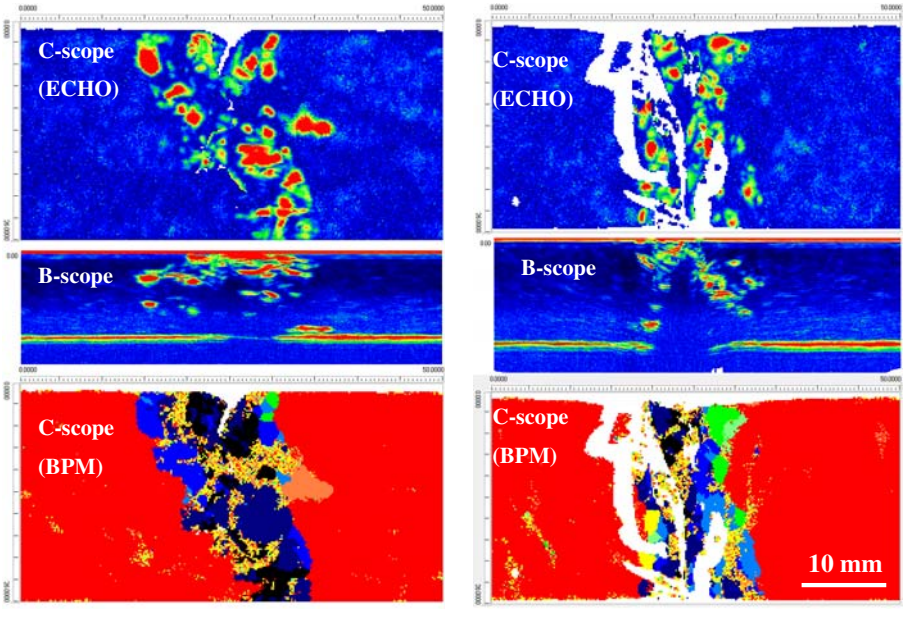

No. 8 No. 10

(c)

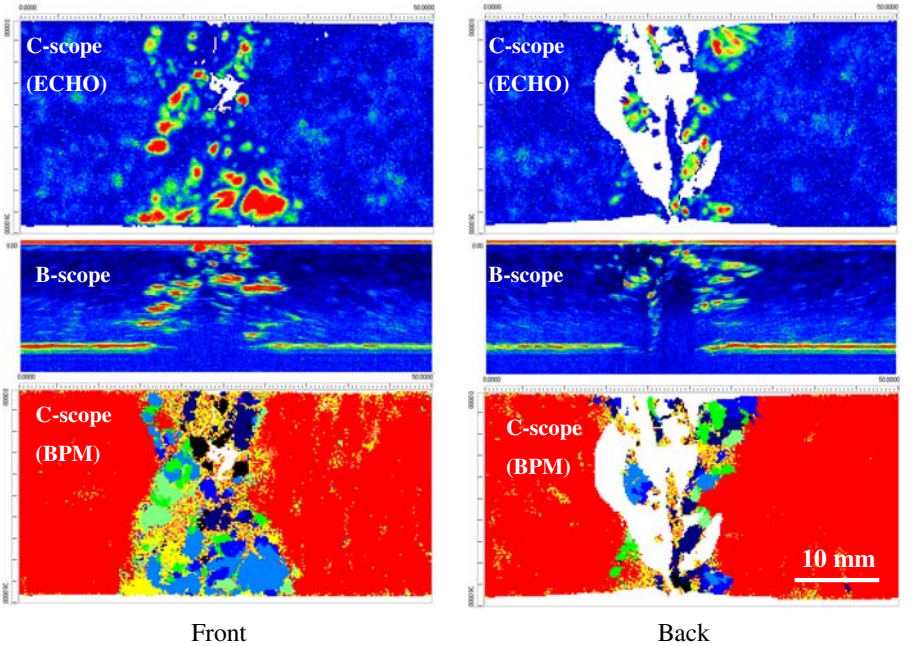

Front Back

(d)

Figure 7. (*Continued*).

Table 3. Impact damage area and TAI strength.

Specimen number	Damage area (mm^2)			TAI strength σ_{TAI} (MPa)
	Front side	Back side	Average	
1	0	0	0	140
2	5.28	11.6	8.41	141
3	8.508	18.7	13.6	173
4	109	131	120	88.4
5	185	135	160	60.6
6	36.8	55.0	46.0	165
7	0.075	0.200	0.138	175
8	93.7	88.1	90.9	165
9	91.3	237	164	43.9
10	105	209	157	N/A*

Note: *No tensile test was conducted for Specimen No. 10 because it was cut for observation of the cross section (see Figure 8).

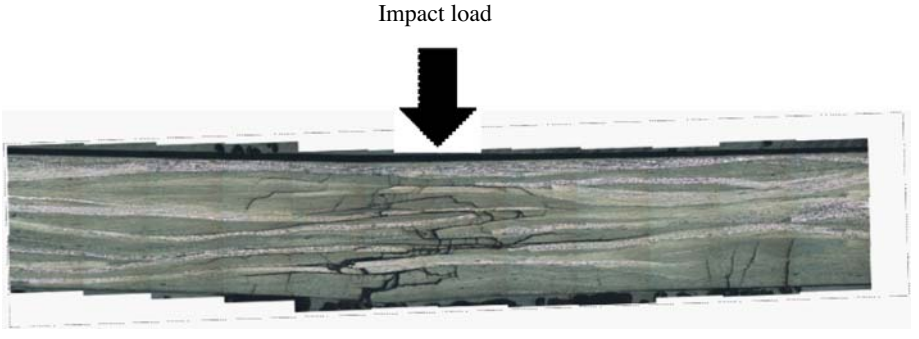

Figure 8. Impact damage observed on the cross section of Specimen No. 10.

correlated with the damage area (see the solid lines in Figure 9(b)–d)). In contrast, the correlation between the maximum load and damage area is considerably low.

3.3. TAI strength and damage evolution

The TAI strength is presented in Table 3 and is plotted against maximum impact load, maximum deflection, incident impact energy, and absorbed energy in Figure 10. Maximum deflection, incident impact energy, and absorbed energy are correlated with the TAI strength to some extent, having thresholds below which the TAI strength remains constant (see the solid and dotted lines in Figure 10(b)–(d)). Figure 11 illustrates tensile stress–strain diagrams of one intact and three impacted specimens. The diagrams for Specimen Nos. 4 and 5 almost overlap that of the intact specimen, although tensile strength and failure strain become lower than those of the intact specimen. This result means that Young's modulus is not reduced even for these two impacted specimens exhibiting strength degradations of 40 and 60%. In contrast, the modulus of Specimen No. 9, retaining only 30% of its original strength, is decreased. However, Young's modulus does not decrease after impact for most of the impacted specimens.

Figure 12 plots the TAI strength against the averaged damage area. The correlation between the TAI strength and damage area is more obvious than in Figure 10. The TAI

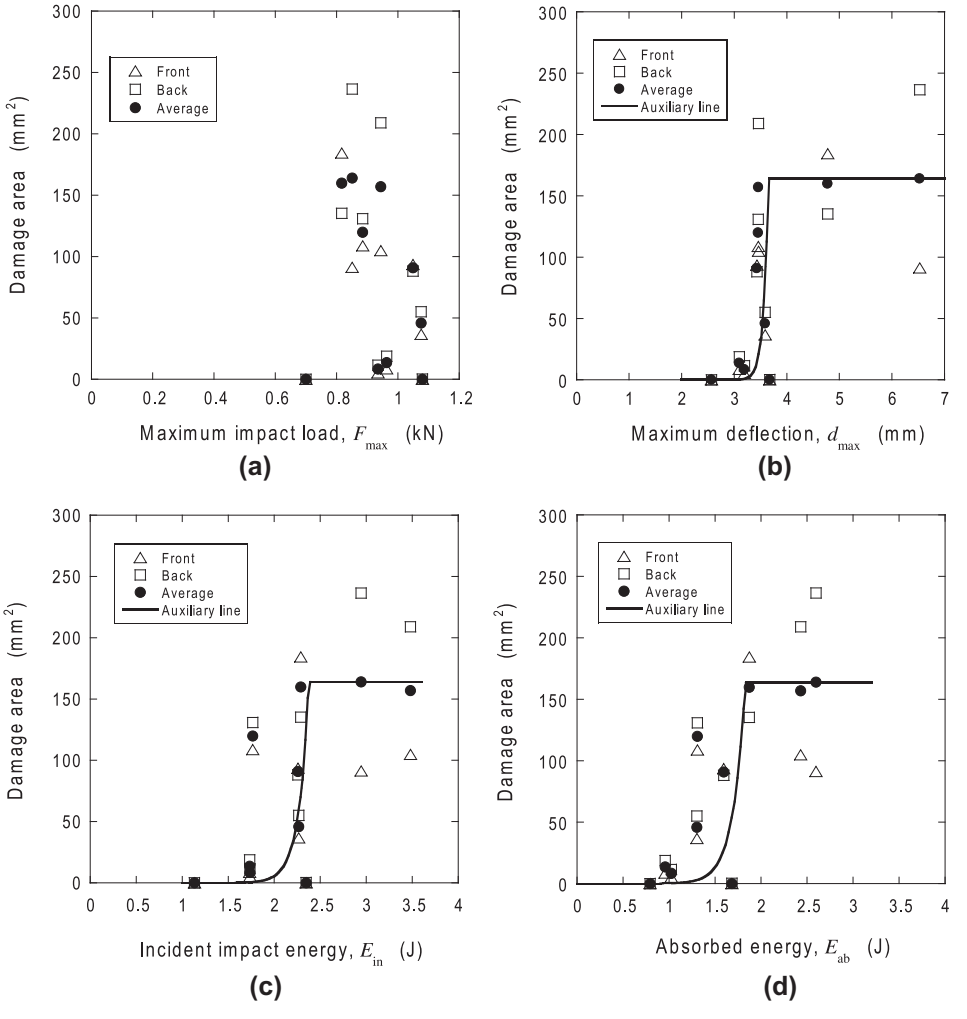

Figure 9. Damage area calculated using C-scan images observed from the front and back surfaces plotted against (a) maximum impact load, (b) maximum deflection, (c) incident impact energy, and (d) absorbed energy.

strength is constant until the damage area reaches a critical value A_C (100 mm^2), above which the TAI strength abruptly decreases.

Figure 13 presents soft X-ray radiographs of damage evolution in Specimen No. 2, and Figure 14 presents those in Specimen No. 8 at several tensile stresses. The observed damage area is smaller than that in the C-scan images (Figures 7(a) and (c)) because a contrast medium was not always injected over the entire damage area. Specimen No. 2 fractures near the right-hand doubler, although the impact damage hardly extends even after final failure (Figure 13). In Specimen No. 8 (Figure 14), final failure occurs around the impact damage that progresses slightly just before the final failure. Figure 15 depicts edge views of damage evolution in Specimen No. 8 loaded in tension. The specimen reached final failure when large-scale damage near the back surface propagated through the thickness. Neither specimen exhibited reduced the TAI strength. In contrast, the impacted specimens with

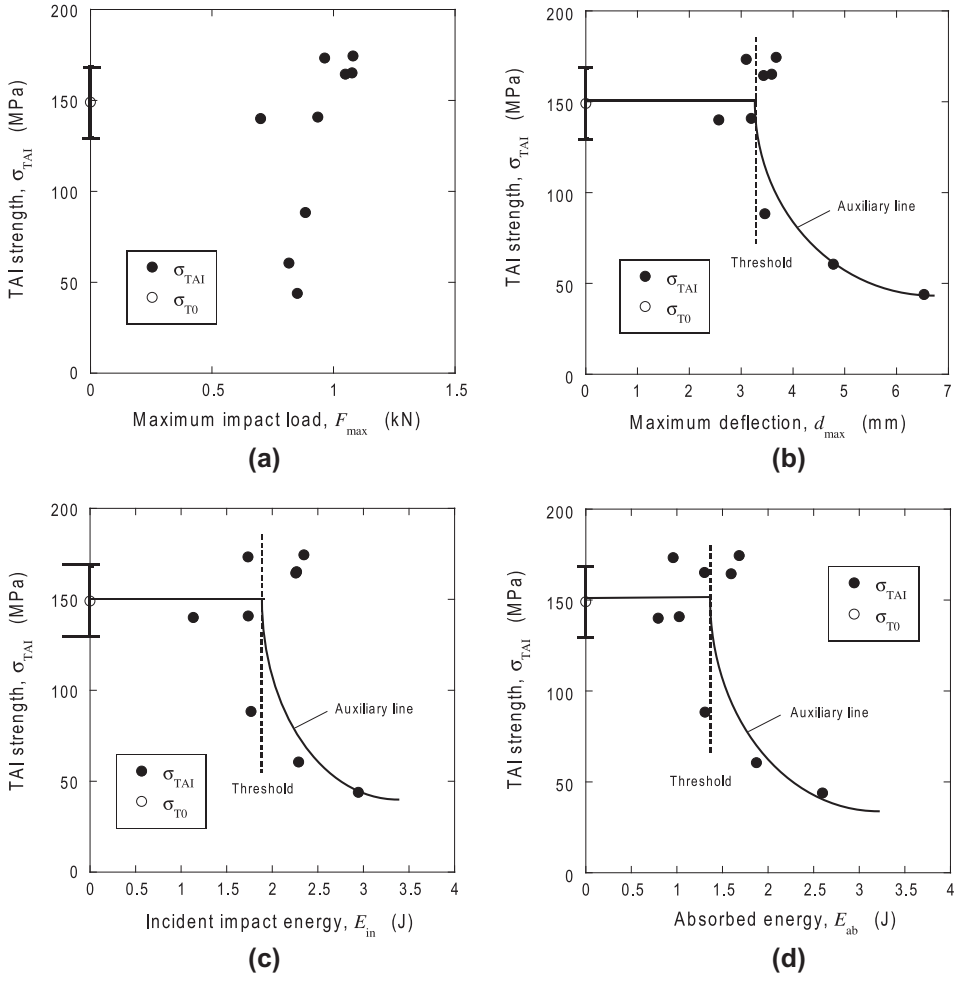

Figure 10. TAI strength vs. (a) maximum impact load, (b) maximum deflection, (c) incident impact energy, and (d) absorbed energy.

damage areas exceeding A_C exhibited final fracture at impact damage and reduction of the TAI strength (Table 3).

These results imply that the TAI strength is dominated only by damage area. However, the TAI strength of the CF-SMC is actually controlled by damage depth. This is because damage area is also correlated with damage depth, as will be described in the next section.

3.4. Fracture-mechanics model

Our previous study [7,8] proved that the strength of the CF-SMC depends on the depth of the *initial damages*, consisting of damage at the edge of strands and the adjacent matrix cracks generated at low stress levels. Therefore, the critical impact load for delamination and the relationship between the TAI strength and impact damage depth are discussed here, assuming that the final failure is caused by delamination propagation. Moreover, we can assume that the original Young's modulus is maintained after impact (Figure 11).

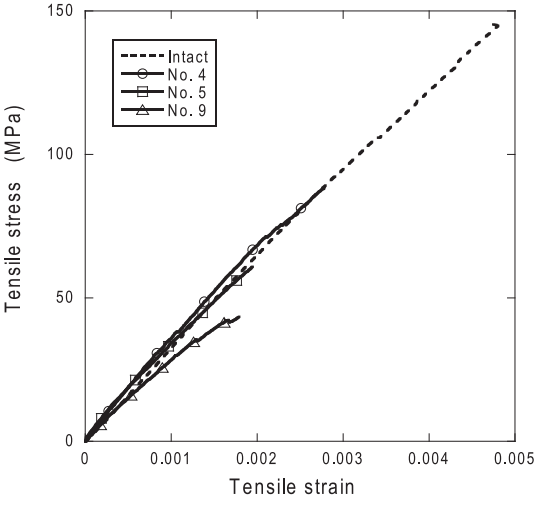

Figure 11. Tensile stress–strain curves for intact and impacted specimens.

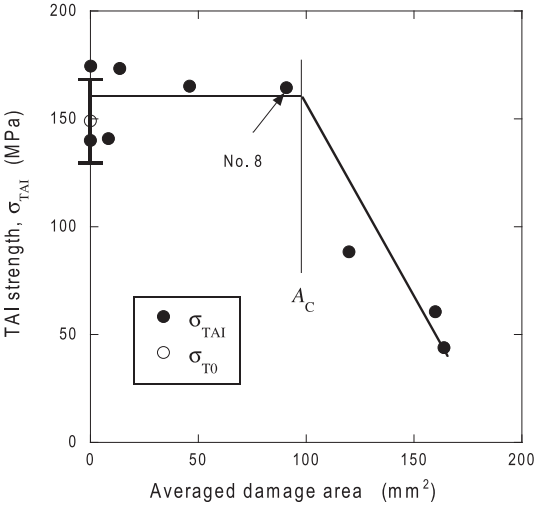

Figure 12. Measured TAI strength vs. averaged damage area. The solid lines are obtained by linear fitting.

According to the models based on fracture mechanics, the tensile and three-point flexural strengths of a nonimpacted CF-SMC specimen are predicted by:

$$\sigma_{T0} = \sqrt{\frac{2\,E_{SMC}(H-h_0)}{H\,h_0}\,G_{IIC}},\ \sigma_{F0} = \frac{b}{b-\delta}\sqrt{\frac{6\,E_{SMC}(H-h_0)}{H\,h_0}\,G_{IIC}} \tag{1}$$

where E_{SMC} denotes Young's modulus, G_{IIC} is mode-II interlaminar fracture toughness, H is half thickness, h_0 is initial damage depth, b is a half span, and δ is the distance of the initial damage from the central line. The average value of δ is a quarter of the strand length (6.35 mm). From Equation (1), we obtain:

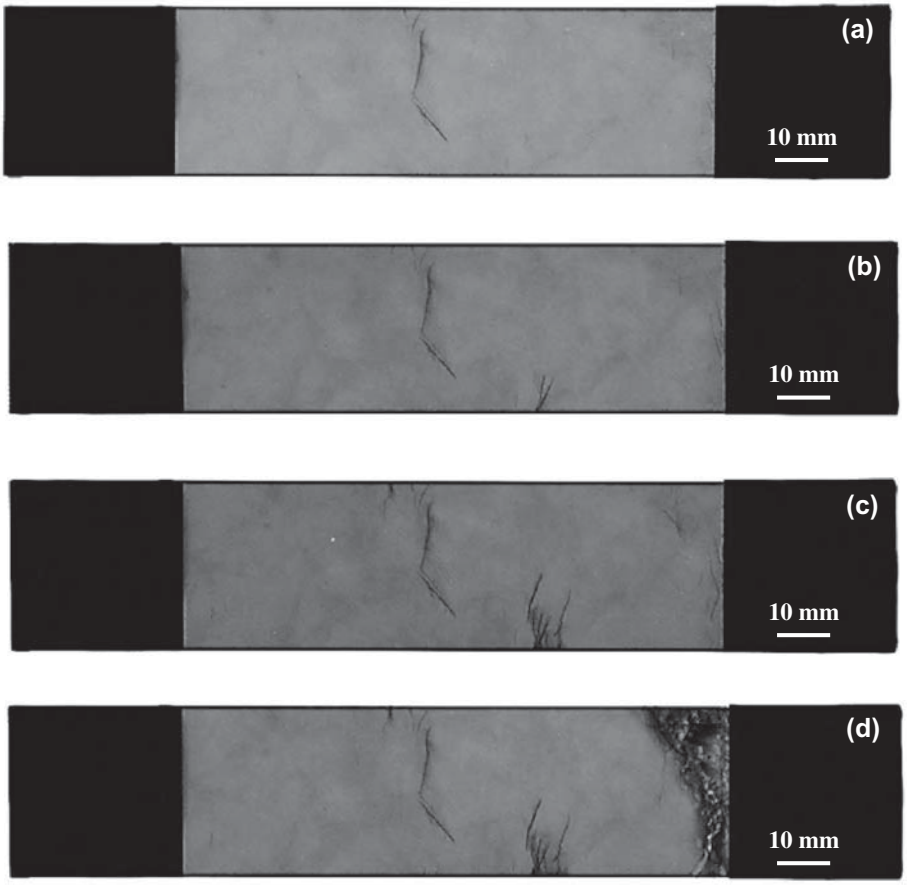

Figure 13. Soft X-ray radiographs of damage evolution in Specimen No. 2 loaded in tension. (a) After Impact, (b) 110 MPa, (c) 140 MPa ,and (d) Fracture (141 MPa).

$$\sigma_{F0} = \frac{\sqrt{3}\, b}{b - \delta}\, \sigma_{T0}. \tag{2}$$

When a specimen regarded as a beam rigidly fixed at both edges is subjected to a three-point impact load, the fracture load is given by:

$$F_C = \frac{2\, W\, t^2\, \sigma_{F0}}{3b} \tag{3}$$

where $t = 2\,H$ is the thickness of the specimen and W is its width. Substituting the material properties and specimen dimensions into Equation (3) leads to $F_C = 1.24$ kN, which exceeds the experiment result (0.8–1.0 kN) in Figure 9(a). It should be noted that the fracture load is overestimated by the present analysis because (i) the load–displacement curve (Figure 4(a)) is nonlinear even for Specimen No. 7 with slight damage and (ii) the actual impact load is applied as a point load, which generates local stress concentration.

Next, the TAI strength of a specimen having impact damage with depth h_i is expressed as:

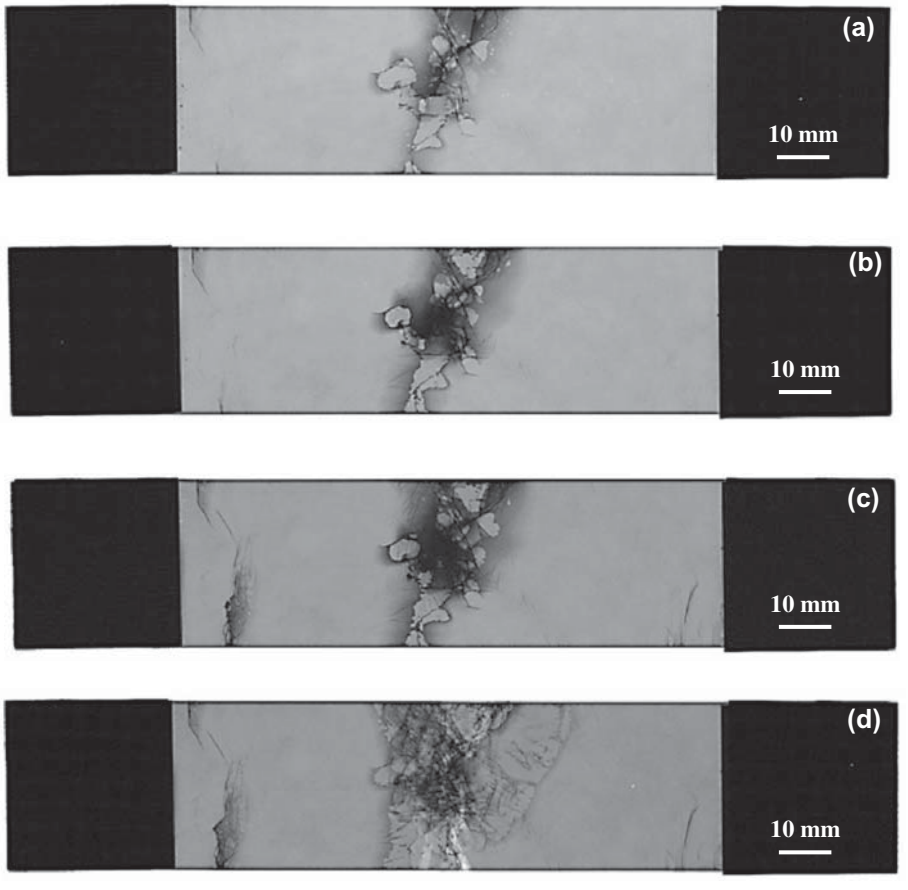

Figure 14. Soft X-ray radiographs of damage evolution in Specimen No. 8 loaded in tension. (a) After Impact, (b) 110 MPa, (c) 160 MPa, and (d) Fracture (164 MPa).

$$\sigma_{\mathrm{TAI}} = \sqrt{\frac{2\,E_{\mathrm{SMC}}(H - h_{\mathrm{i}})}{H\,h_{\mathrm{i}}}\,G_{\mathrm{IIC}}}. \tag{4}$$

From Equations (1) and (4), we obtain:

$$\frac{h_{\mathrm{i}}}{H} = \frac{h_0}{h_0 + (H - h_0)\,r^2} \tag{5}$$

where $r = \sigma_{\mathrm{TAI}}/\sigma_{\mathrm{T0}}$ denotes the residual-to-initial strength ratio. Substituting the properties in Table 1 into Equation (1), we obtain $h_0/H = 0.55$. It was demonstrated in our previous study [7,8] that this value is reasonable. Accordingly, h_{i}/H can be calculated for a given value of r using Equation (5). Calculated h_{i}/H is plotted against the TAI strength and averaged damage area in Figure 16. The impact damage depth h_{i}/H decreases monotonically with increasing the TAI strength (Figure 16(a)). In contrast, the impact damage depth is kept approximately constant for a damage area smaller than A_{C} (Figure 16(b)). However, it increases and approaches unity as damage area becomes larger than A_{C}. Impact damage depth measured from the B-scope images (Figure 7) and the optical micrographs (Figures 8 and 15) are also plotted in Figure 16.

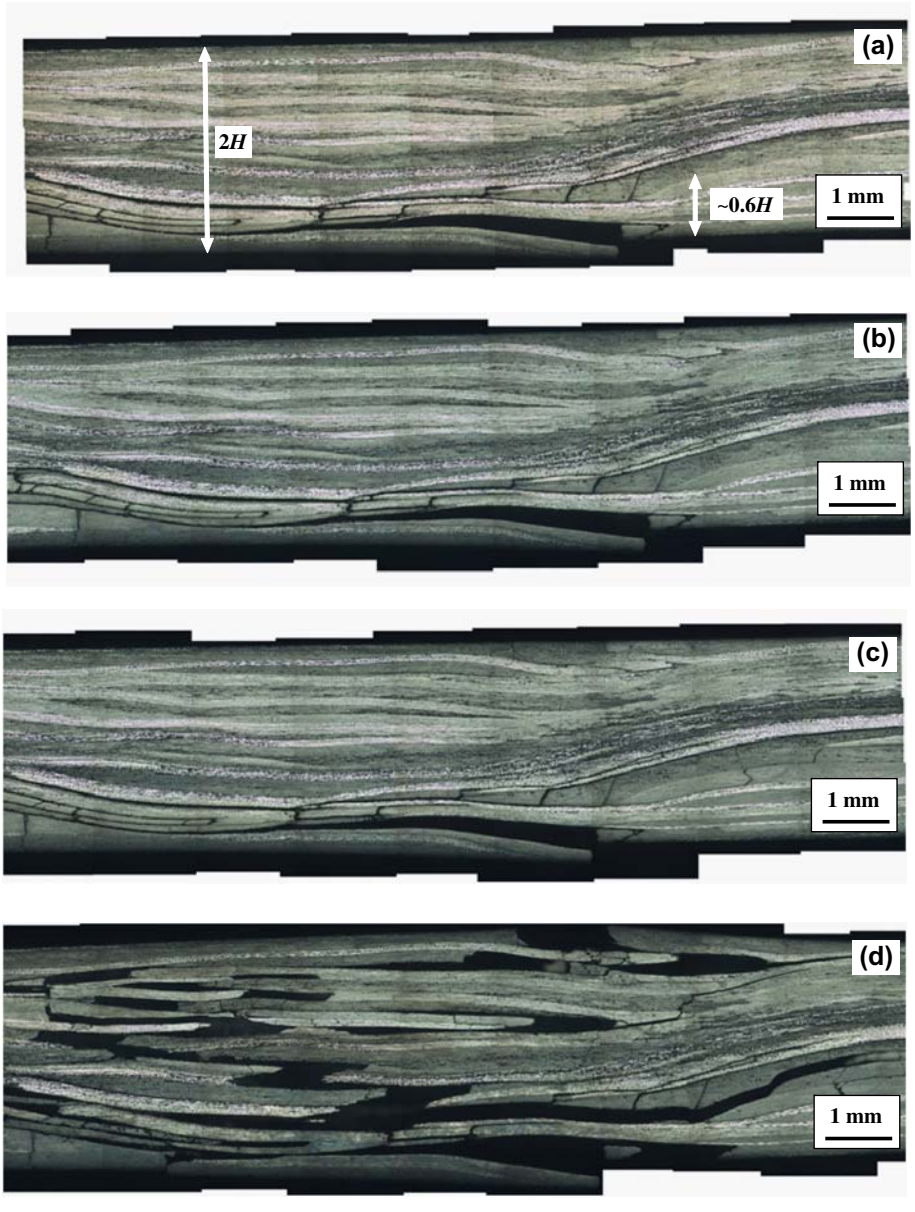

Figure 15. Edge views of damage evolution in Specimen No. 8 loaded in tension. (a) After Impact, (b) 100 MPa, (c) 160 MPa, and (d) fracture (164.5 MPa).

Although the damage depth obtained from the B-scope images has some scatter, measured data are in reasonably good agreement with predictions using Equation (5). For example, in Specimen No. 8 with no strength degradation, h_i/H is predicted to be 0.50. The experiment result in Figure 15(a) ($h_i/H = 0.6$) confirms the reasonableness of this prediction.

It is concluded that the impact damage depth dominates the TAI strength. Since the damage depth is correlated with damage area, it is also related to impact energy. When the impact energy exceeds a critical or threshold, the damage tends to extend in the thickness direction by way of matrix cracks and strand edges, rather than in the in-plane direction as delamination.

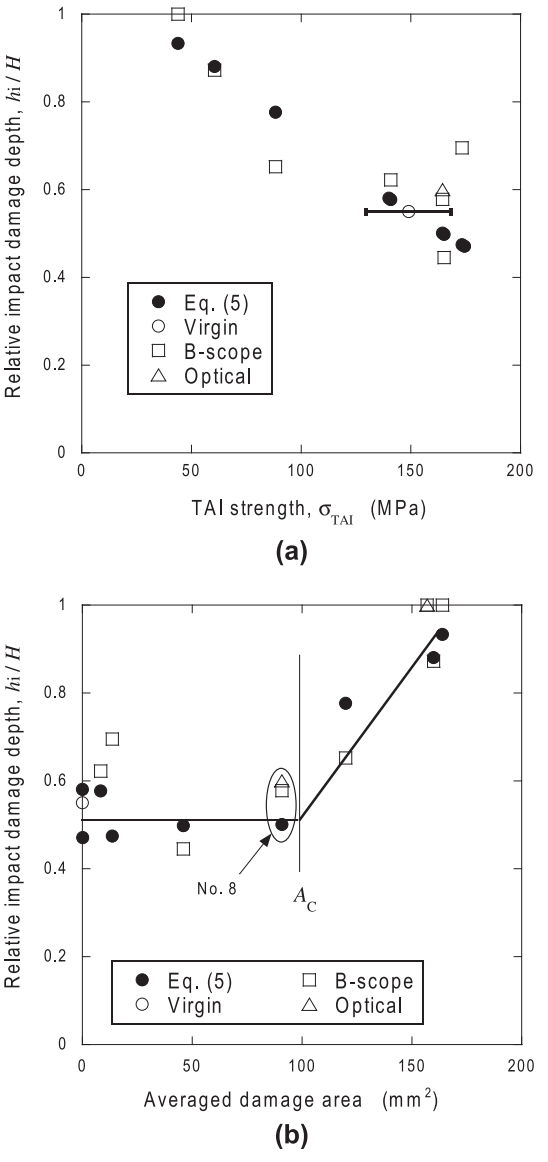

Figure 16. Measured and calculated relative impact damage depth vs. (a) TAI strength and (b) averaged damage area. The solid lines in (b) are obtained by linear fitting of the plots calculated using Equation (5).

Consequently, the impact damage depth becomes greater than the initial depth; as a result, the TAI strength decreases. Conversely, when impact energy is less than the critical energy, the TAI strength remains at the initial strength, as long as the damage depth remains constant.

4. Conclusions

The impact damage and the TAI strength of a CF-SMC composite were investigated. Impact damage states were quantitatively characterized using ultrasonography and optical microscopy to relate the damage area with incident and absorbed energy and maximum impact deflection.

The TAI strength was also correlated with these parameters. Consequently, a clear correlation between the TAI strength and damage area was identified. However, the TAI strength was found to be expressed as a function of initial and impact damage depth based on fracture mechanics. Hence, damage extension in the in-plane and thickness directions must be considered for estimating the TAI strength. In addition, the critical impact load for delamination was predicted using flexural strength.

Acknowledgment

The authors express their appreciation to Toray Industries, Inc. for the offer of SMC specimens. The authors also thank Dr Shu Minakuchi of Tokyo University for his technical support in impact testing. This research is partly supported by a Grant-in-Aid (No. 21360417) for Scientific Research of the Ministry of Education, Science, Sports and Culture of Japan.

References

[1] Jēkabsons N, Fernberg SP. Prediction of progressive fracture of SMC by application of bridging laws. Compos. Sci. Technol. 2003;63:2133–2142.
[2] Fernberg SP, Jēkabsons N. Determination of bridging laws for SMC materials from DENT tests. Compos. Sci. Technol. 2003;63:2143–2153.
[3] Marissen R, Linsen J. Variability of the flexural strength of sheet moulding compounds. Comp. Sci. Technol. 1999;59:2093–2100.
[4] Morozov EV, Morozov KE, Selvarajalu V. Damage model development for SMC composites. Comp. Struct. 2003;62:373–378.
[5] Suzuki H, Sekine H. Study of fracture energy and fracture behavior of short-fiber-reinforced SMC composites on the basis of micromechanics. JSME Int. J. Series A. 1995;38:111–115.
[6] Fitoussi J, Guo G, Baptiste D. A statistical micromechanical model of anisotropic damage for SMC Composites. Compos. Sci. Technol. 1998;58:759–763.
[7] Ogi K, Yamanouchi M. A simple fracture mechanical model for predicting tensile strength of a SMC composite. J. Japan Soc. Compos. Mater. 2010;36:198–204.
[8] Ogi K, Yamanouchi M. Temperature dependence of flexural strength of a CF-SMC composite. Appl. Compos. Mater. 2011;18:397–408.
[9] Taketa I, Okabe T, Kitano A. A new compression-molding approach using unidirectionally arrayed chopped strands. Compos. A. 2008;39:1884–1890.
[10] Taketa I, Okabe T, Kitano A. Strength improvement in unidirectional arrayed chopped strands with interlaminar toughening. Compos. A. 2009;40:1174–1178.
[11] Kau HT. A study on the impact behavior of chopped fiber reinforced composite. Polym. Compos. 1990;11:253–264.
[12] Lee S-M, Cheon J-S, Im Y-T. Experimental and numerical study of the impact behavior of SMC plates. Compos. Struct. 1999;47:551–561.
[13] Dear JP, Brown SA. Impact damage processes in reinforced polymeric materials. Compos. A. 2003;34:411–420.
[14] Centeno G, Benítez FG, Wideberg JP. Experimental study of impact on SMC composites used in the automotive industry. Int. J. Vehicle Design. 2007;44:282–292.
[15] Palmer J, Savage L, Ghita OR, Evans KE. Sheet moulding compound (SMC) from carbon fibre recyclate. Compos. A. 2010;41:1232–1237.
[16] Chaturvedi SK, Sierakowski RL. Residual strength assessment of SMC composites subjected to dynamic impact. Compos. Struct. 1983;1:137–161.
[17] Gu ZL, Sun CT. Reduction of flexural properties in an SMC composite due to impact. J. Reinforced Plastics Compos. 1987;6:13–24.
[18] Briggs TM, Ramulu M. Edge finishing effects on the impact behavior of chopped GFRP composites. Exp. Mech. 2010;50:321–331.
[19] Uda N, Ono K, Kunoo K. Compression fatigue failure of CFRP laminates with impact damage. Compos. Sci. Technol. 2009;69:2308–2314.